Measurements of low-mode asymmetries in the areal density of laser-direct-drive deuterium–tritium cryogenic implosions on OMEGA using neutron spectroscopy

C. J. Forrest,[1,a)] A. Crilly,[2] A. Schwemmlein,[1] B. Appelbe,[2] M. Gatu-Johnson,[3] R. Betti,[1] J. P. Knauer,[1] V. Yu. Glebov,[1] V. Gopalaswamy,[1] O. M. Mannion,[1] Z. L. Mohamed,[1] P. B. Radha,[1] S. P. Regan,[1] C. Stoeckl,[1] and W. Theobald[1]

[1]*Laboratory for Laser Energetics, University of Rochester, Rochester, New York,14623-1299 USA*
[2]*Centre for Inertial Fusion Studies, The Blackett Laboratory, Imperial College, South Kensington Campus, London, UK*
[3]*Plasma Science and Fusion Center, Massachusetts Institute of Technology, Cambridge, Massachusetts, 02139 USA*

(Presented XXXXX; received XXXXX; accepted XXXXX; published online XXXXX)
(Dates appearing here are provided by the Editorial Office)

Areal density is one of the key parameters that determines the confinement time in inertial confinement fusion experiments, and low-mode asymmetries in the compressed fuel are detrimental to the implosion performance. The energy spectra from scattering of the primary deuterium–tritium (DT) neutrons off the compressed cold fuel assembly are used to investigate low-mode nonuniformities in direct-drive cryogenic DT implosions at the Omega Laser Facility. For spherically symmetric implosions, the shape of the energy spectrum is primarily determined by the elastic and inelastic scattering cross sections for both neutron-deuterium (nD) and neutron-tritium (nT) kinematic interactions. Two highly collimated lines of sight, which are positioned at nearly orthogonal locations around the OMEGA target chamber, record the neutron time-of-flight signal in current mode. An evolutionary algorithm is being used to extract a model-independent energy spectrum of the scattered neutrons from the experimental neutron time-of-flight data and is used to infer the modal spatial variations ($\ell = 1$) in the areal density. Experimental observations of the low-mode variations cold-fuel assembly ($\rho L_0 + \rho L_1$) show good agreement with a recently developed model, indicating a departure from a spherical symmetry of the compressed DT fuel assembly. Another key signature in the presence of a low-mode variation is the broadening of the kinematic end-point due to anisotropy of the dense fuel conditions has been observed.

I. INTRODUCTION

In direct-drive inertial confinement fusion (ICF) ignition designs, a cryogenic deuterium–tritium (DT) shell surrounding a vapor and encapsulated in a thin plastic ablator (<10 μm) is symmetrically illuminated with nominally identical laser beams on the OMEGA Laser System.[1] In these target designs, the incident laser ablates the thin shell, which then launches one or multiple shocks through the remaining converging shell and into the vapor region. The shock-transit stage of the implosion is followed by a deceleration phase, where the kinetic energy of the converging shell is converted to the internal energy of the hot spot.[2] At peak compression, the temperature and density is sufficient to initiate thermonuclear fusion reactions of the DT fuel.[3] To achieve conditions relevant for ignition implosion designs, the hot-spot size must exceed the mean free path of fusing ions to remain confined in the dense plasma. This requirement is essential to maximize the energy deposition of the alpha particle in the hot spot and surrounding cold fuel. Targets that are not compressed symmetrically will be unable to fully convert their shell kinetic energy to hot-spot thermal energy, reducing the overall fusion yield generated from the implosion.

Nuclear diagnostics are essential to interpreting the condition of the DT fuel during the compression phase in ICF experiments.[4,5] Measurable parameters that determine performance of ICF implosions include the ion temperature (T_i), areal density (ρL), and the primary DT neutron yield (Y_n) (Ref. 6). Furthermore, the energy spectra from scattering of the primary neutrons off the compressed target is used to investigate low-mode nonuniformities in cryogenic DT implosions. The shape of the neutron energy spectrum is fully determined by the elastic and inelastic scattering cross section as compared to spherically symmetric targets shell conditions.[7] Deviations from a symmetric implosion are expected to lead to a decrease in target performance metrics including the yield and 4π average areal density.

In this paper, we describe the two highly collimated neutron time-of-flight detectors that exist on OMEGA and the technique that has been developed to extract a model-independent energy spectrum. Using the resulting neutron energy spectrum, a reconstruction technique demonstrates the 3-D map of the compressed fuel near peak compression and provides a more-complete understanding into the symmetry of laser-direct-drive implosions. In the kinematic limit, DT fusion neutrons that undergo direct elastic backscatter from ions lose the largest fraction of their energy possible for a single scattering event. This scattering event produces a sharp edge in the neutron energy spectrum at the kinematic end point for both nD and nT. For stationary

[a)]Author to whom correspondence should be addressed: cforrest@lle.rochester.edu.

target ions, the resultant edge energy is dependent only on the ion mass and incoming neutron energy. It will be shown that the spectral shape is dependent on the scattering rate-weighted ion velocity distribution and variation in the areal density.[8] These techniques will be demonstrated using data from an experiment with a large mode-1 drive asymmetry. Finally, we discuss the optimal lines of sight with an additional neutron spectrometer that would be required on OMEGA in order to greatly reduce the uncertainties in the 3-D interpretation of the compressed fuel assembly.

II. DISTRIBUTION OF NEUTRONS GENERATED IN A COMPRESSED TARGET

The primary neutron distribution generated once an ICF implosion has reached temperature and densities sufficient to produce thermonuclear reactions consists of the DD, TT, and DT fusing ions and can be expressed by

$$\frac{\mathrm{d}N}{\mathrm{d}E} = Y_{\mathrm{n}}\left[\left(\mathrm{DT} + \frac{1}{2}\frac{f_{\mathrm{d}}}{f_{\mathrm{t}}}\frac{\langle\sigma v_{dd}\rangle}{\langle\sigma v_{\mathrm{dt}}\rangle}\mathrm{DD} + \frac{f_{\mathrm{t}}}{f_{\mathrm{d}}}\frac{\langle\sigma v_{\mathrm{tt}}\rangle}{\langle\sigma v_{\mathrm{dt}}\rangle}\mathrm{TT}\right)\right], \quad (1)$$

where Y_{n} is the primary DT yield, f_{d} and f_{t} are the fuel fraction of the fuel, and $\langle\sigma v\rangle$ is the reactivity rate with the associated fusing pair of ions. Once the primary reactions take place, a small fraction of the neutrons produced within the compressed fuel will scatter throughout the ~30-μm hot-spot radius, and the ~10-μm-thick dense fuel region. These secondary reactions include both the elastic and inelastic scattering contributions that account for <5% of the primary signal. The contributions from the secondary reactions are defined by

$$\frac{\mathrm{d}N}{\mathrm{d}E} = Y_{\mathrm{n}}\left[\rho L N_{\mathrm{A}}\frac{\sigma_{\mathrm{nd}}f_{\mathrm{d}} + \sigma_{\mathrm{nt}}f_{\mathrm{t}} + \sigma_{\mathrm{D(n,2n)}p}f_{\mathrm{d}} + \sigma_{\mathrm{T(n,2n)D}}f_{\mathrm{t}}}{f_{\mathrm{d}}m_{\mathrm{d}} + f_{\mathrm{t}}m_{\mathrm{t}}}\right], \quad (2)$$

where N_{A} is the Avogadro constant, σ is the differential ($\mathrm{d}\sigma/\mathrm{d}E$) and double-differential ($d^2\sigma/\mathrm{d}\Omega\mathrm{d}E$) cross section. The total energy spectrum includes both the primary and secondary contributions and is expressed as

$$\frac{\mathrm{d}N}{\mathrm{d}E} = \frac{\mathrm{d}N}{\mathrm{d}E}(\mathrm{primary}) + \frac{\mathrm{d}N}{\mathrm{d}E}(\mathrm{secondary}). \quad (3)$$

The resultant energy spectrum assumes a symmetric fuel distribution at peak compression. In experiments, several factors can introduce perturbations including target offset, ice-layer nonuniformity, and laser-beam energy imbalance, which has been shown to result in variations of the dense fuel. Information about the asymmetry of the dense region is embedded in the energy spectrum and is a direct mapping between the cosine of the neutron-scattering angle and the residual energy of the outgoing neutron. This results in the number of scattered neutrons in a particular neutron energy range containing information on the areal density along a specific neutron-scattering angle and therefore a specific region of the dense fuel. A model to where the differential and double-differential cross-sections are modified to better describe this variation in the cold fuel is with assuming a low-mode (ℓ = 1) distribution as given by

$$\frac{\mathrm{d}\sigma}{\mathrm{d}E} = \int\left(\frac{\mathrm{d}\sigma}{\mathrm{d}\Omega}\right)\left(1 + \frac{\Delta\rho L}{\rho L} * \cos\theta\right)\mathrm{d}E, \quad (4)$$

$$\frac{\mathrm{d}\sigma_{\mathrm{n,2n}}}{\mathrm{d}E} = \int 2\pi\frac{d^2\sigma}{\mathrm{d}E\mathrm{d}\Omega}\left(1 + \frac{\Delta\rho L}{\rho L} * \cos\theta\right) \times \mathrm{d}\cos\theta. \quad (5)$$

Here the addition of the $\Delta\rho L/\rho L$ allows for the shape of the energy spectrum below the primary DT signal to follow a mode-1 distribution. In practice, a high-dynamic-range spectrometer is required to observe this neutron signal several orders of magnitude below the primary DT reaction.[9]

III. HIGH-DYNAMIC-RANGE NEUTRON TIME-OF-FLIGHT SPECTROMETERS

To measure neutron spectra over a dynamic range of 10^6 while maintaining sensitivity in the instrument, several difficulties must be considered. For example, the dominant primary DT peak accounts for more than 90% of the neutron energy deposited in the spectrometer. Such a large impulse incident on the spectrometer will produce a long-light afterglow component in the scintillator. This causes the lower-energy neutrons in the detector to be masked by the afterglow component from the primary peak that is still present from the scintillation process. Another consideration for high-yield DT implosions is the neutron scattering from the target chamber walls and surrounding concrete structures. One method employed to achieve a high signal-to-background with minimal light afterglow was a double-collimated line of sight with a low-light afterglow scintillator.[10] Ultrafast gating microchannel-plate photomultiplier tubes (MCP-PMT's) were implemented to gate out the primary DT peak to measure the low-energy neutron spectrum.

To meet these requirements, spectrometers were designed to utilize an advanced scintillator compound with low-afterglow characteristics used to minimize the masking of additional neutron components after the dominant primary DT peak. The diagnostic consists of a 2-mm-thick stainless-steel cylindrical housing that is 20 cm in diameter and 10-cm deep, which contains the scintillation fluid. Thin (<0.5-cm) stainless-steel plates are used to seal the cylindrical housing to minimize neutron attenuation normal to the line of sight. In this study, two identical four-MCP-PMT's are positioned 13.4 and 22.1 m from target chamber center on the OMEGA Laser System, as shown in Fig. 1.

Scintillation light from the incident neutrons are viewed through fused-silica windows, where the light is coupled to four 40-mm-diam PMT's.[6] The instrument needs to be positioned close enough to achieve high-neutron statistics but far enough away to interpret the individual components of the energy spectrum. The signals from the PMT's are recorded by a 1-GHz Tektronix® DPO-7104

digital oscilloscope. A 3-D drawing of the spectrometers used along the P7 and H10 line of sight is shown in Fig. 2.

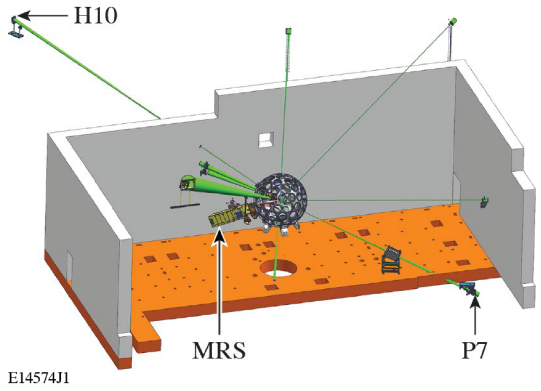

FIG. 1. Two highly collimated lines of sight on the OMEGA Laser System located outside the Target Bay concrete shielding along the P7 and H10 ports. The blue structure is the OMEGA Target Chamber and the green lines are projected to the neutron time-of-flight spectrometers at distances of 13.4 and 22.1 m, respectively. The magnetic recoil spectrometer (MRS) that measures the scattered neutrons using a knock-on deuteron technique is mounted directly in the OMEGA target chamber.

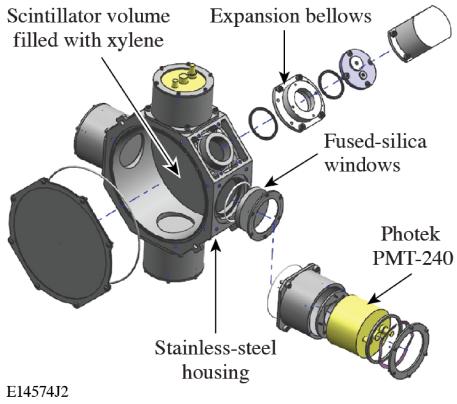

FIG. 2. A CAD drawing of the neutron time-of-flight (nTOF) detector shows a cavity for the scintillation fluid, the fused-silica windows, and the photomultiplier tube (PMT) mounts.

These spectrometers have the unique ability to measure the primary neutron energy spectrum and the down-scattered portion of the neutron energy spectrum (1 to 15 MeV). Due to detector resolution constraints, the forward-scattered region (8 to 12 MeV) is not fully resolved and is not discussed in this analysis. The areal density is inferred by measuring the number of scattered neutrons is currently in the 3- to 8-MeV region of the scattered neutron spectrum that corresponds to neutrons with an average scattering cosine of $\mu = -0.75$ to 0.50. Therefore, the neutron time-of-flight (nTOF) spectrometers infer the areal density in the region of the target along the opposing (backscattered region) detectors' lines of sight. An alternative approach used to measure the scattered neutrons depends on a knock-on deuteron technique.

A magnetic recoil spectrometer (MRS) is mounted directly on the OMEGA target chamber uses incident neutrons emitted from the target that elastically scatter off of a CD_2 conversion foil, which results in the production of recoiled deuterons. The recoiled deuterons exit forward and are directed through the aperture of the magnet, which are spatially dispersed as they propagate through the magnetic field due to their different velocities. A CR-39 array is positioned to record the incident deuterons as a function of the deflection angle that is directly related to the recoil energy.[11]

The setup of the MRS detector on OMEGA measures the primary DT neutron energy spectrum and the forward-scattered portion of the neutron energy spectrum (9 to 11 MeV). Due to detector resolution limitations, only the primary DT fusion yield is currently able to be accurately inferred from the primary DT spectrum. In this approach, the areal density is inferred by measuring the number of primary DT neutrons as compared to the signal in the 9- to 11-MeV region of the scattered neutron spectrum that corresponds to neutrons with an average scattering cosine of $\mu = 0.4$ to 0.7. A computer model of the MRS detector mounted on the target chamber is shown in Fig. 1. With the two highly collimated nTOF's and the MRS, a large fraction of the scattered neutrons from a compressed target are observed. A representation of the coverage for each spectrometer is shown in Fig. 3.

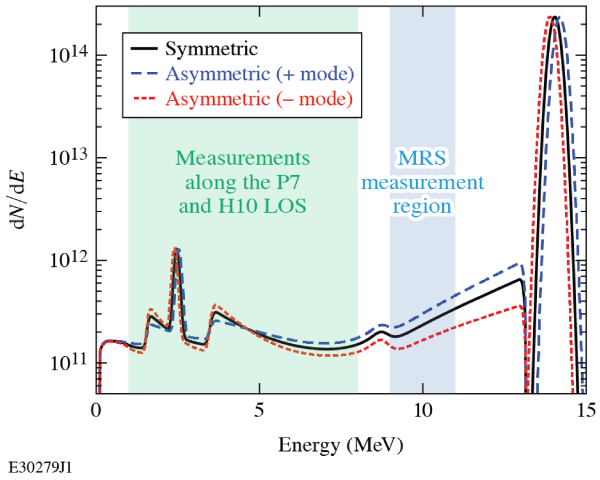

FIG. 3. The two highly collimated lines of sight measure the neutrons that scatter off the backside the target in the energy region from 1 to 8 MeV, shown in two spherical sections (shaded in green). A third diagnostic measures the energy spectrum in a 9- to 11-MeV band (shaded in blue). Examples of low mode asymmetries for both a positive mode (blue dashed) and negative mode (red dashed) l=1 that would be present in the energy spectrum as viewed by the spectrometer are shown.

An additional effect observed in the energy distribution is the mean energy shift in the primary DT and DD peak distributions. The shift in the primary peak is due to the hot-spot flow which has been shown to be a strong correlation in the direction of the minimum areal density.

The main advantage of evaluating the spectrum over an extended region is to interrogate the scattered neutrons for variations in the dense fuel assembly. An example of the modal variation that would be expected in the energy spectrum from the scattered neutrons is shown in Fig. 3 with a positive and negative mode $\ell = 1$. Due to the limited energy region, it would be challenging for the current MRS to extract variations in the energy spectrum because of modal

perturbations in the ~10-MeV energy region. Over the extended energy region, this model illustrates the motivation to use the scattered neutron energy spectrum to understand the effects of areal-density asymmetries.

IV. MODEL-INDEPENDENT ENERGY SPECTRUM

The nTOF on OMEGA operates in current mode and measures the neutron flux incident on the detector. The time record is directly related to the energy of the emitted neutron with the exact distance of the detector to the source. Traditional forward-fitting requires a model for the data and may thereby introduce undesired biases to the analysis. A new concept uses a user-defined number of node points to construct a continuous-energy spectrum by interpolation. This technique is commonly referred to as a genetic or evolutionary algorithm.

A. Evolutionary algorithm

A distinct advantage of this evolutionary algorithm (EA) is the ability to include all of the known quantities of the experimental setup and detection system (nTOF). The general formalization for the EA can be expressed by

$$I(t)=\left[\varepsilon_{\text{scint}}(E)\,\varepsilon_{\text{los}}(E)\frac{\mathrm{d}N}{\mathrm{d}E}\frac{\mathrm{d}E}{\mathrm{d}t}\right]\otimes R(E,t), \qquad (7)$$

where $\varepsilon_{\text{scint}}(E)$ is the light sensitivity of the scintillator, $\varepsilon_{\text{los}}(E)$ the attenuation for the associate line of sight, dNdE is the neutron energy spectrum, dNdt is the Jacobian, and $R(E,t)$ is the response function of the detection system.

With $I(t)$, the time-of-flight signal is forward fitting using novel machine-learning concepts. The effects of attenuation along the flight path, scintillator sensitivity, and the PMT instrument response according to Eq. (7) are applied to this hypothetical spectrum before they are converted to time space and compared to the experimental signal. This iterative approach is expressed by

$$\frac{\mathrm{d}N_1}{\mathrm{d}E}\rightarrow\sum\frac{\left[I(t)_{\text{signal}}-I(t)_1\right]^2}{I(t)_1}=\chi_1^2, \qquad (8)$$

$$\frac{\mathrm{d}N_2}{\mathrm{d}E}\rightarrow\sum\frac{\left[I(t)_{\text{signal}}-I(t)_2\right]^2}{I(t)_2}=\chi_2^2 \qquad (9)$$

when

$$\chi_1^2<\chi_2^2\rightarrow\frac{\mathrm{d}N_1}{\mathrm{d}E}, \qquad (10)$$

$$\chi_1^2>\chi_2^2\rightarrow\frac{\mathrm{d}N_3}{\mathrm{d}E}, \qquad (11)$$

where $\mathrm{d}N_3/\mathrm{d}E$ is the next iteration of the energy spectrum. The χ^2 value from this comparison is used as a fitness-parameter to evaluate the quality of the solution before a node is changed randomly and the process is repeated to deliver a second χ^2. The solution with the smaller χ^2 is taken for the next iteration, and the procedure is repeated until χ^2 reaches a plateau. Several adjustments have been made and tested to this basic evolutionary algorithm to prevent overfitting, which was also described in a similar algorithm.[12] It was found that a very effective way to limit overfitting is nested fitting. The fit starts with a small number of nodes, to which more nodes are added one at a time. For each fit, the χ^2 value is allowed to reach a plateau, after which another point is included at a random energy and the fitting procedure is repeated. Using parallel computing, several spectra with different node points are fitted simultaneously, and the fit with the smallest χ^2 is the basis for including the next point. A minor drawback with this technique is the required computational time to execute the fitting routine. Currently, the analysis for each spectrum can take up to a day to complete when utilizing a high-speed computing cluster in the OMEGA theory group.

B. Monte Carlo simulations

For each iteration, the fitting routine requires the detector light sensitivity and the line-of-sight attenuation for the specified spectrometer along the P7 and H10 locations. These detector effects are modeled using a neutron transport code, namely MCNP. The simulations show that the primary DT neutron detectors on OMEGA, the detector sensitivity, and line-of-sight attenuation do not vary significantly across the narrow (<1-MeV) range of neutron energies analyzed by these detectors as shown in Fig. 4. For the primary DD and scattered-neutron detectors, the MCNP calculations reveal that the detector sensitivity can vary 10%–20% below 4 MeV, while the line-of-sight attenuation can vary ~5% across the energy ranges that are analyzed. Therefore, in the analysis of the raw time-of-flight spectra, the exact shape of the detector sensitivity and line-of-sight attenuation are included.[13]

V. DATA ANALYSIS

The two lines of sight from each spectrometer have an inherent background that is due to the residual neutron scattering from the environment, such as the target chamber and surrounding steel and concrete structures necessary to hold the mirror assemblies. An approach to infer this background contribution is with dedicated experiments, evaluating the shape of the scattered neutrons with implosions that have minimal areal density. In this study, we looked at thin CH shells and exploding pushers with apparent temperatures below 6 keV to mitigate any kinetic effects that lead to yield ratio anomalies and inaccurate distributions of the primary reactions.

Once the background has been accounted for, the remaining model-independent energy spectrum is used to extract key implosions metrics. A fit to the data uses using Eq. (3) with the modal variation addition in Eqs. (4) and (5) provides an areal density ρL_0 and variation ρL_1 for the P7 and H10 lines of sight

$$\rho L_{\text{los}}(\Omega)=\rho L_0+\rho L_1\Omega\cdot\hat{\mu}_{\text{hs}},$$

where

$$\rho L_1=\frac{\Delta\rho L\times\rho L_0}{\Omega_{\text{det}}\cdot\hat{\mu}_{\text{hs}}}$$

with the required inputs such as the primary DT yield, apparent ion temperature, and fuel fraction used to fill the targets. Preliminary fits (not shown) indicated that the region between the D_2 peak (2.45 MeV) and the nT kinematic end point (3.52 MeV) underestimated the experimental data is believed to be due to the contribution from the triton breakup that was not initially included in the analysis.

Earlier experimental energy spectra of protons and deuterons produced in accelerator experiments from the triton breakup reactions, T(n,2n)D and T(n,3n)p, were barely significant (deuterons) and not significant (protons) given the experimental uncertainties, respectively.[14] It is unknown if other experimental data for these reactions have been published. The shape of the energy spectrum for the double differential cross section was calculated using the Evaluated Nuclear Data File (ENDF) LAW = 6. The cross section for this reaction has been calculated to be 19 mb (Ref. 15).

An example of a fit to the experimental data from an experimental campaign in October of 2021 is shown in Figs. 4 and 5 for the P7 and H10 locations.

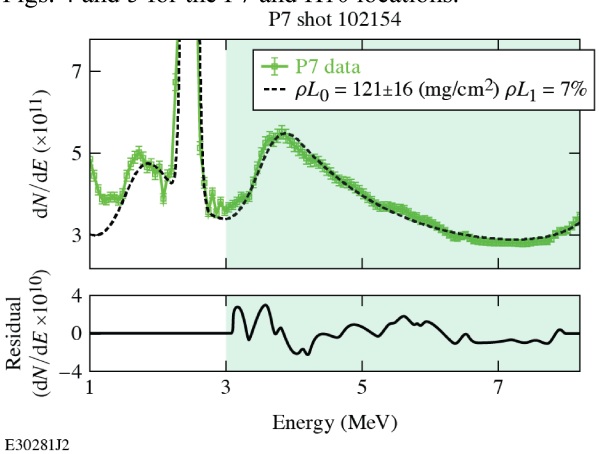

FIG. 4. A fit to the experimental data with the statistical uncertainty and the model (dashed black line) in the energy region from 3 to 8 MeV along the P7 line of sight. Below the D_2 peak at 2.45 MeV, the nD kinematic endpoint is observed.

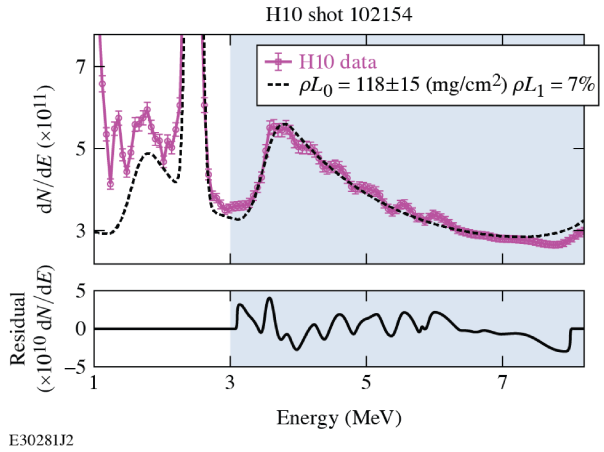

FIG. 5. A fit to the experimental data (purple) with the statistical uncertainty and the model (dashed black line) in the energy region from 3 to 8 MeV along the H10 line of sight. In this spectrometer, the region below the D_2 peak, is less resolved and the nD kinematic end point is as evident when compared to the P7 line of sight (see Fig. 4).

The fit region is shown from 3 to 8 MeV. The energy region from 1 to 8 MeV is resolved in the P7 location. However, the region below the D_2 peak along the H10 line of sight is not well resolved due to a larger background contribution. During the October 2021 campaign, there were five experiments with the experimental values listed in Table I.

TABLE I: Experimental values from October 2021.

Shot #	ρL_0 (P7) (mg/cm^2)	ρL_1	ρL_0 (H10) (mg/cm^2)	ρL_1	v_{hs} (km/s)
102145	105±12	0.01	101±11	0.32	45
102149	98±11	0.03	95±11	0.26	51
102154	118±13	0.03	111±13	0.09	66
102158	107±12	0.12	105±12	0.10	75
102162	116±13	0.24	112±13	0.09	100

The best performer in this campaign was shot 102154, which had a $Y_n = 2.22 \times 10^{14}$ and the highest ρL and the lowest variation along both lines of sight. The worst performer of the day was shot 102162 that had an $Y_n = 1.79 \times 10^{14}$ and a significant hot-spot flow and an observed low mode. To better understand how the variation in the areal density impacts implosion performance, an accurate reconstruction of the areal-density distribution over 4π is required.

To reconstruct the areal density using the inferred values, ($\rho L_0 + \rho L_1$) several radiation-hydrodynamic simulations, along with recent experiments on OMEGA, have shown that there are strong correlations between the direction of the measured hot-spot velocity and the areal-density asymmetry direction. It is expected that the direction of minimum areal density is expected to be along the direction of the hot-spot velocity. As a result, a mode $\ell = 1$ areal-density distribution and the direction of the hot-spot flow is expressed by

$$\rho L(\Omega) = \overline{\rho L_0} + \overline{\rho L_1}\Omega \cdot \hat{v}_{hs}, \tag{12}$$

where $\overline{\rho L_0}$ and $\overline{\rho L_1}$ are the mean values of the areal density and variation in the areal density projected along the hot-spot flow velocity $\hat{v}_{hs}$ is measured by independent detectors.[16] An example of the reconstruction of the areal density from the implosions with a significant mode 1 is shown in Fig. 6. With the minimum areal density directed just below the P7 axis, there is up to a factor of 2 in variation of the dense fuel.

To further constrain the inferred areal density a comparison between the MRS and the nTOF is shown in Fig. 7. In this comparison the arithmetic mean from the nTOF measurements is calculated by integrating the overall reconstructed areal-density values from

$$\rho L_{am} = \frac{1}{4\pi}\int \rho L \, d\theta d\varphi. \tag{13}$$

To achieve this reconstruction without an assumption on the direction of the low mode (i.e., $\ell = 1$), up to four

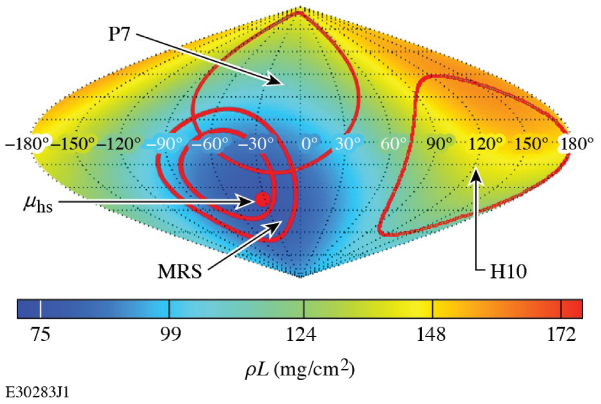

FIG. 6. A reconstruction of the areal density using the P7 and H10 neutron spectrometers. Due to the limited number of spectrometers the minimum areal density is constrained to be directed along the direction of the hot-spot flow vector μ_{hs} noted by the red dot.

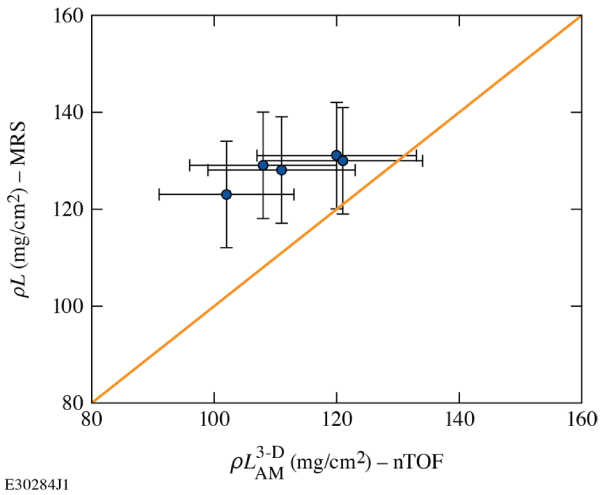

FIG. 7. The arithmetic mean from the 3-D reconstruction is compared to the areal density inferred from the MRS spectrometer.

spectrometers are required to measure the scattered neutron spectra. Therefore, with four strategically highly collimated lines of sight, a reconstruction of the areal-density distribution over 4π can be inferred without an assumption on the direction of the low mode.[17]

It is believed that low-mode asymmetry in a directly driven ICF implosion's potential performance is a limiting factor. A recent model demonstrates that an asymmetric-piston description can be used to show the impact of mode-1 shell asymmetry and degradation in performance.[18] In this model, the increase in areal-density variation is correlated with yield degradation and is expressed by

$$\frac{Y}{Y_{LILAC}} = \left(1 - f^2\right)^a,$$

where a is given to be 3.3 and f is the variation in the areal density and is expressed by

$$f = \frac{\rho L_{max} - \rho L_{min}}{\rho L_{max} + \rho L_{min}}$$

with ρL_{max} and ρL_{min} obtained from the 3-D reconstruction technique. As with the increase in the the variation in the areal density, a minimal correlation with yield degradation is observed. However, with the variation in the areal density compared to the measured yield and divivded by the 1-D *LILAC* yield is up to 40% lower as shown in Fig. 8 with the solid black line. This can be explained by other mechanisms that degrade the yield that are not associated with the variation in the areal density.

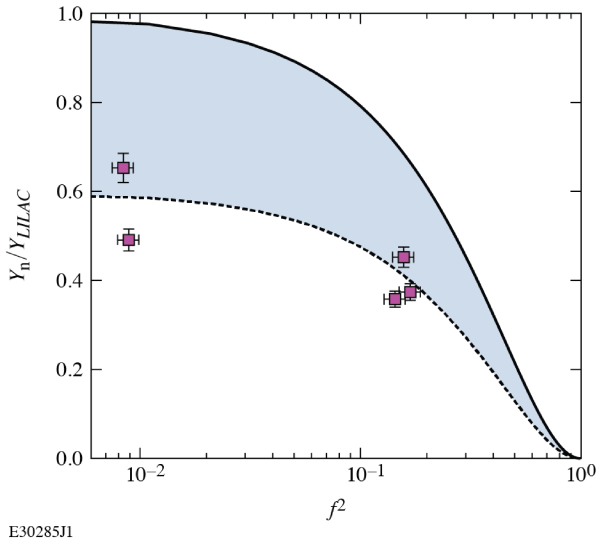

FIG. 8. The increase in areal-density variation from the experimental campaign shows a minimal correlation with yield degradation. A reduction in overall performance of ~40% (shaded region) is likely due to other degradation mechanisms such as target offset, ice-layer nonuniformity, and laser-beam energy imbalance.

In the presence of a mode-1 asymmetry, the kinematic edge broadening is a key signature indicating that the accelerated ion moves slower in the higher areal-density region. The kinematic limit for single scattering of neutrons produced in D–T fusion reactions produces a backscatter edge in the measured neutron spectrum. The shape of the energy spectrum of the backscattered neutrons is dependent on the scattering ion-velocity distribution. A recent study showed that as the neutrons scatter in the dense cold fuel, the neutron-backscatter edge presented a novel measurement of the hydrodynamic conditions at stagnation. The spectral shape of the edge is determined by the scattering rate-weighted fluid velocity and temperature of the dense DT fuel layer during neutron production. A model of this edge broadening is shown in Fig. 9.

Measurements on the broadening of the kinematic edges (Fig. 10) show qualitative agreement with the anisotropy of the dense fuel conditions from separate lines of sight.

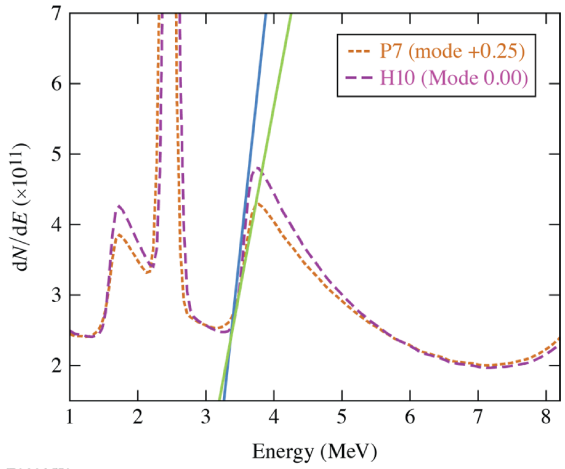

E30285J2

FIG. 9. A model illustrates the broadening of the kinematic edge due to the anisotropy of the cold fuel depending on the spectrometers line-of-sight.

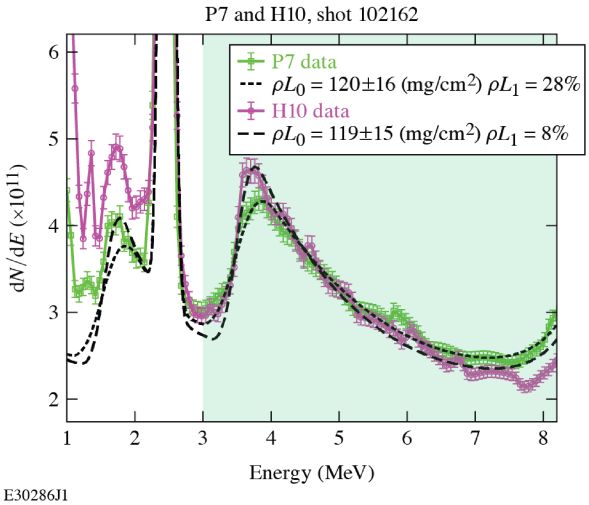

E30286J1

FIG. 10. An example of a cryogenic implosion with a significant mode 1 that shows qualative agreement with the broadening of the kinematic edge due to the anisotropy of the cold fuel depending on the spectrometers line of sight as predicted by the model.

VII. SUMMARY

In this manuscript, a novel approach was introduced using an evolutionary algorithm is used to extract a model-independent energy spectrum of the scattered neutrons from the experimental neutron time-of-flight data. This technique allows for a more-detailed analysis of the scattered spectra required to infer the modal spatial variations ($\ell = 1$) in the compressed fuel. Experimental observations of the low-mode variations of the cold fuel assembly ($\rho L_0 + \rho L_1$) show good agreement with a recently developed model, indicating a departure from a spherical symmetry of the compressed DT fuel assembly. The inclusion of the deuteron and triton breakup in the implosion target are non-negligible and are treated in the inference of the areal density. In one example with a significant mode, the hot-spot flow was projected along the region with the lowest areal density. The addition of two more highly collimated lines of sight is required to reconstruct the areal density in 4π without an assumption on the direction of the low mode.

In addition to the inferred areal density, the shape of the nT kinematic edge does indicate a change along the separate lines of sight due to anisotropy of the dense fuel conditions. A correlation of this difference in the broadening does have a non-negligible correlation with the flow of the hot spot.

ACKNOWLEDGMENT

This work was supported by the U.S. Department of Energy Office of Inertial-Confinement Fusion under cooperative agreement No. DE-NA0003856, the University of Rochester, and the New York State Energy Research and Development Authority.

This report was prepared as an account of work sponsored by an agency of the U.S. Government. Neither the U.S. Government nor any agency thereof, nor any of their employees, makes any warranty, express or implied, or assumes any legal liability or responsibility for the accuracy, completeness, or usefulness of any information, apparatus, product, or process disclosed, or represents that its use would not infringe privately owned rights. Reference herein to any specific commercial product, process, or service by trade name, trademark, manufacturer, or otherwise does not necessarily constitute or imply its endorsement, recommendation, or favoring by the U.S. Government or any agency thereof. The views and opinions of authors expressed herein do not necessarily state or reflect those of the U.S. Government or any agency thereof.

REFERENCES

1. T. R. Boehly *et al.*, Opt. Commun. **133**, 495 (1997).
2. J. Nuckolls, L. Wood, A. Thiessen, and G. Zimmerman, Nature **239**, 139 (1972).
3. H. Brysk, Plasma Phys. **15**, 611 (1973).
4. V. Yu. Glebov, C. Stoeckl, T. C. Sangster, C. Mileham, S. Roberts, and R. A. Lerche, Rev. Sci. Instrum. **77**, 10E712 (2006).
5. C. J. Forrest, V. Yu. Glebov, V. N. Goncharov, J. P. Knauer, P. B. Radha, S. P. Regan, M. H. Romanofsky, T. C. Sangster, M. J. Shoup, and C. Stoeckl, Rev. Sci. Instrum. **87**, 11D814 (2016).
6. O. M. Mannion *et al.*, Phys. Plasmas **28**, 042701 (2021).
7. A. J. Crilly, B. D. Appelbe, O. M. Mannion, C. J. Forrest, and J. P. Chittenden, Phys. Plasmas **28**, 022710 (2020).
8. A. J. Crilly, B. D. Appelbe, O. M. Mannion, C. J. Forrest, V. Gopalaswamy, C. A. Walsh, and J. P. Chittenden, Phys. Plasmas **27**, 012701 (2020).
9. C. J. Forrest *et al.*, Rev. Sci. Instrum. **83**, 10D919 (2012).
10. R. Lauck, M. Brandis, B. Bromberger, V. Dangendorf, M. B. Goldberg, I. Mor, K. Tittelmeier, and D. Vartsky, IEEE Trans. Nucl. Sci. **56**, 989 (2009).
11. J. A. Frenje *et al.*, Rev. Sci. Instrum. **79**, 10E502 (2008).
12. E. P. Hartouni, B. Beeman, J. A. Caggiano, C. Cerjan, M. J. Eckart, G. P. Grim, R. Hatarik, A. S. Moore, D. H. Munro, T. Phillips, and D. B. Sayre, Rev. Sci. Instrum. **87**, 11D841 (2016).
13. R. Hatarik *et al.*, J. Appl. Phys. **118**, 184502 (2015).
14. J. M. Kootsey, Nucl. Phys. A **113**, 65 (1968).
15. A. Deltuva and A. C. Fonseca, Phys. Rev. C **86**, 011001(R) (2012).
16. O. M. Mannion, J. P. Knauer, V. Yu. Glebov, C. J. Forrest, A. Liu, Z. L. Mohamed, M. H. Romanofsky, T. C. Sangster, C. Stoeckl, and S. P. Regan, Nucl. Instrum. Methods Phys. Res. A **964**, 163774 (2020).
17. F. Weilacher, P. B. Radha, and C. Forrest, Phys. Plasmas **25**, 042704 (2018).
18. O. A. Hurricane, D. T. Casey, O. Landen, D. A. Callahan, R. Bionta, S. Haan, A. L. Kritcher, R. Nora, P. K. Patel, P. T. Springer, and A. Zylstra, Phys. Plasmas **29**, 012703 (2022).